PAPER

Check for updates

Bromoargentate/g-C$_3$N$_4$ heterojunction by *in situ* growth: 2-D bromoargentate framework with a transition metal complex linker and cocatalyst for enhanced photocatalytic activity *via* g-C$_3$N$_4$ hybrid†

Yiming Tian, Taohong Ren, Hongjin Zhu and Dingxian Jia ⬤ *

A 2-D bromoargentate hybrid [{Cu(phen)}$_2$(μ-OH)$_2$(Ag$_3$Br$_5$)]$_n$ (phen = 1,10-phenanthroline) (**1**) was prepared by the reaction of Cu(NO$_3$)$_2$·3H$_2$O, AgBr, KBr and phen in a C$_2$H$_5$OH/DMF mixed solvent under solvothermal conditions. In compound **1**, three tetrahedral AgBr$_4$ units are interconnected into a 1-D [Ag$_3$Br$_5$]$_n$ chain by edge-sharing. The [Ag$_3$Br$_5$]$_n$ chains were linked by tetranuclear [{Cu(phen)}$_2$(μ-OH)$_2$]$_2$ complex units *via* Cu–Br bonds to form the layered bromoargentate hybrid [{Cu(phen)}$_2$(μ-OH)$_2$(Ag$_3$Br$_5$)]$_n$. The [{Cu(phen)}$_2$(μ-OH)$_2$(Ag$_3$Br$_5$)]$_n$ layers were successfully loaded on the surface of g-C$_3$N$_4$ by *in situ* growth under the same solvothermal conditions, and a **1**/g-C$_3$N$_4$ heterojunction was formed. The **1**/g-C$_3$N$_4$ heterojunction exhibited a stable and reproducible photocurrent response with a photocurrent density of 23.68 μA cm^{-2}, which is 2.65 and 8.05 times greater than those of parent **1** and g-C$_3$N$_4$, respectively. The degradation conversion of crystal violet (CV) reached 98.0% on the photocatalyst of **1**/g-C$_3$N$_4$ heterojunction after light irradiation for 60 min. The **1**/g-C$_3$N$_4$ heterojunction exhibited a much higher photocatalytic efficiency than did **1** and g-C$_3$N$_4$ for CV degradation, which suggested that the synergistic effect between **1** and g-C$_3$N$_4$ in the heterojunction promoted photocatalytic performance. The investigation of the catalytic mechanism showed that all h$^+$, ·OH and ·O$_2^-$ species are reactive substances in the photodegradation.

Introduction

The environmental pollution caused by wastewater has attracted widespread attention due to the increasing amount of organic pollutants, such as organic dyes, antibiotics, and pesticides discharged into water, with an increasing population and industrialization.[1] Organic pollutants might have a series of harmful impacts on the environment and human health due to their chemical toxicity and nonbiodegradability. To meet the need for clean and safe water, various wastewater treatment technologies, such as screening, filtration, and centrifugal separation, are conventionally used.[2] Currently, there is increasing interest in using photocatalytic techniques to eliminate organic pollutants in wastewater. Photocatalytic degradation is an environmentally friendly and economical wastewater treatment method, in which sunlight energy is used to convert organic pollutants into small molecules or nontoxic substances.[3] In recent years, organic–inorganic halometallate hybrid materials, especially iodoargentate hybrids, have been promising candidate photocatalysts for the degradation of organic pollutants in wastewater treatment. The polymeric iodoargentate hybrids (EtPPh$_3$)Ag$_3$I$_4$ (Et = ethyl), (*n*-PrPPh$_3$)Ag$_3$I$_4$ (*n*-Pr = *n*-propyl), (i-PrPPh$_3$)Ag$_5$I$_6$ (i-Pr = isopropyl), and [(Me)$_2$-2,2′-bipy]Ag$_8$I$_{10}$ (Me = methyl, 2,2′-bipy = 2,2′-bipyridine) exhibited photocatalytic efficiencies for the degradation of the organic dyes rhodamine B (RhB) and methyl orange (MO) in wastewater under visible light irradiation.[4,5] The TM-complexes containing iodoargentate hybrids, K$_x$[TM(2,2′-bipy)$_3$]$_2$Ag$_6$I$_{11}$ (TM = Fe, Co, Ni, Zn; *x* = 0.89–1), [Ni(2,2′-bipy)$_3$][H-2,2-bipy]Ag$_3$I$_6$, [TM(phen)$_3$]$_2$Ag$_{11}$I$_{15}$·H$_2$O (phen = 1,10-phenanthroline) (TM = Co, Cu), and [TM(phen)$_3$]$_2$Ag$_{13}$I$_{17}$ (TM = Co, Cd) were photocatalytically active in the degradation of crystal violet (CV) and RhB.[6,7] The degradation conversions of CV reached 56–92% after 60 min of visible light irradiation, while the degradation conversions of RhB were in the range of 29–80% after 180 min of light irradiation. The photocatalytic activities of halometallate

College of Chemistry, Chemical Engineering and Materials Science, Soochow University, No. 199 Renai Road, Suzhou, 215123, P. R. China.
E-mail: jiadingxian@suda.edu.cn

† Electronic supplementary information (ESI) available: Selected bond lengths and angles, IR spectra, structural figures, PXRD, SEM, EDS, XPS, solid-state UV-vis reflectance spectra, photocurrent response, and photocatalytic measurements. CCDC reference numbers 2347788 for **1**. For ESI and crystallographic data in CIF or other electronic format see DOI: https://doi.org/10.1039/d4ce00510d

hybrids are affected by various factors, such as the composition, structure, optical bandgap, and electron-accepting ability of counter cations.[7,8] The compositions and structures of halometallate hybrid materials are influenced by various factors during preparation, such as the features and charge distributions of counter cations, ligands to the metal centers, and guest solvent molecules.[9] A large number of iodoargentate hybrids with different compositions and structures have been prepared using organic cations, transition metal (TM), and lanthanide (Ln) metal complex cations as counter cations or structural directing agents.[10–12] However, the photocatalytic activity and stability of the iodoargentate hybrid materials need to be enhanced for the purpose of application.

Since the 2-D polymeric semiconductor g-C$_3$N$_4$ (graphitic carbon nitride) was used as a metal-free conjugated photocatalyst for H$_2$ evolution in 2006,[13] g-C$_3$N$_4$ has been considered a next-generation semiconductor photocatalyst due to its unique triazine ring structure, tunable band gap (normal band gap of ~2.7 eV), high physicochemical stability, excellent photoelectrochemical properties, and low cost.[14] G-C$_3$N$_4$ can be easily prepared by the thermal polycondensation of several inexpensive precursors, such as cyanamide, dicyandiamide, melamine, urea, thiourea, and ammonium thiocyanate.[14c,15] As a 2-D polymeric semiconductor, g-C$_3$N$_4$ can construct various cocatalysts with well-matched energy levels of other semiconductors to form heterostructures. Many g-C$_3$N$_4$-based composites with different components and compositions have been prepared by loading metals,[16] metal oxides,[17] or metal sulfides[18] on the surface of g-C$_3$N$_4$ layers. In recent years, the synthesis of g-C$_3$N$_4$-based semiconductor cocatalysts by loading metal organic frameworks (MOFs) has attracted increasing interest.[19] Yue prepared a Ni-MOF-based nanocomposite of UNiMOF/g-C$_3$N$_4$, which exhibited enhanced photocatalytic H$_2$ production under visible light irradiation.[20] Lu and Zolfigol constructed Ti-MOF/g-C$_3$N$_4$, and Zr-MOF/g-C$_3$N$_4$ heterojunctions for the photocatalysis of the coupling of primary amines and the Gomberg–Bachmann–Hey reaction.[21] Very recently, we prepared a g-C$_3$N$_4$/[Pb(18-crown-6)(PbAg$_2$I$_6$)]$_n$ (18-crown-6 = 1,4,7,10,13,16-hexaoxacyclooctadecane) heterocomposite by doping the layered heterometallic Pb-iodoargentate hybrid [Pb(18-crown-6)(PbAg$_2$I$_6$)]$_n$ with g-C$_3$N$_4$.[22] The heterocomposite exhibited synergistically enhanced photocatalytic activity for MB degradation. In this work, we designed and synthesized a layered bromoargentate [{Cu(phen)}$_2$(μ-OH)$_2$(Ag$_3$Br$_5$)]$_n$ (**1**), and prepared the first g-C$_3$N$_4$/bromoargentate heterojunction of **1**/g-C$_3$N$_4$ by loading the [{Cu(phen)}$_2$(μ-OH)$_2$(Ag$_3$Br$_5$)]$_n$ layer on the surface of g-C$_3$N$_4$ via an in situ growth method. The photoelectric and photocatalytic properties of the **1**/g-C$_3$N$_4$ heterojunction were investigated.

Results and discussion

Syntheses

Crystals of **1** suitable for X-ray single-crystal structure measurements were obtained by the reaction of Cu(NO$_3$)$_2$·3H$_2$O, AgBr, KBr and phen in a C$_2$H$_5$OH/DMF mixed solvent under solvothermal conditions. The same reaction in the sole C$_2$H$_5$OH solvent failed to produce compound **1**, indicating that DMF played an important role in the crystallization of compound **1**. In the FT-IR spectra of **1**, the absorption bands at 2800–2900 cm^{-1} are attributed to C–H vibrations. The bands at approximately 1580–1520 cm^{-1} are due to the stretching vibrations of the C≡N bond (Fig. S1†). The wide bands at 3578 (m) and 3447 (s) in **1** are attributed to the vibrations of the O–H bonds involved in hydrogen bonding. The PXRD patterns of as-prepared **1** are consistent with the simulated XRD patterns based on the single-crystal XRD data (Fig. 1), indicating that the bulk phase of as-prepared compound **1** was pure. The **1**/g-C$_3$N$_4$ heterojunction was prepared in situ by synthesis of **1** in the presence of g-C$_3$N$_4$ powder. In the FT-IR spectrum of the **1**/g-C$_3$N$_4$ heterojunction, the absorption peaks at 805, 1233, 1314, 1395, and 1626 cm^{-1} are attributed to the typical stretching mode for the CN-heterocyclic system of g-C$_3$N$_4$,[18a,23] while the main absorption bands of **1** are almost unchanged (Fig. S1†). A broad peak at 27.3° appeared in the PXRD pattern of the **1**/g-C$_3$N$_4$ heterojunction, which was indexed as the characteristic peak of g-C$_3$N$_4$,[18a,23,24] while the peak positions of **1** were unchanged (Fig. 1). SEM images of the as-prepared g-C$_3$N$_4$ and **1**/g-C$_3$N$_4$ heterojunction are shown in Fig. 2. The g-C$_3$N$_4$ has an irregular laminar structure with frilled and wrinkled sheets on its surface (Fig. 2a). The **1**/g-C$_3$N$_4$ heterojunction micrographs exhibited distribution and deposition of **1** rod-like microcrystals on the surface of the g-C$_3$N$_4$ nanosheets (Fig. 2b and c). EDS analysis revealed the presence of C, N, O, Br, Cu and Ag in the obtained **1**/g-C$_3$N$_4$ heterojunction (Fig. 2d), confirming the coexistence of **1** and g-C$_3$N$_4$. The results of FT-IR, PXRD, SEM and EDS measurements confirmed that the **1**/g-C$_3$N$_4$ heterojunction was successfully prepared by in situ growth under solvothermal conditions.

Crystal structure of 1

Compound **1** crystallizes in the triclinic space group $P\bar{1}$ with two formular units in the unit cell (Table S1†). Its asymmetric unit is composed of three Ag, five Br and two Cu atoms, two phen molecules, and two OH groups (Fig. 3a). All the Ag atoms
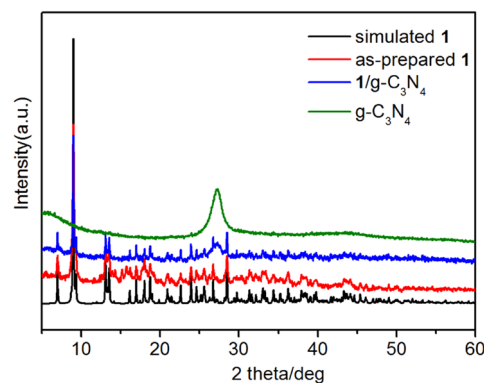

Fig. 1 Simulated XRD pattern of **1**, and experimental powder XRD patterns of as-prepared **1**, g-C$_3$N$_4$, and **1**/g-C$_3$N$_4$ heterojunction.
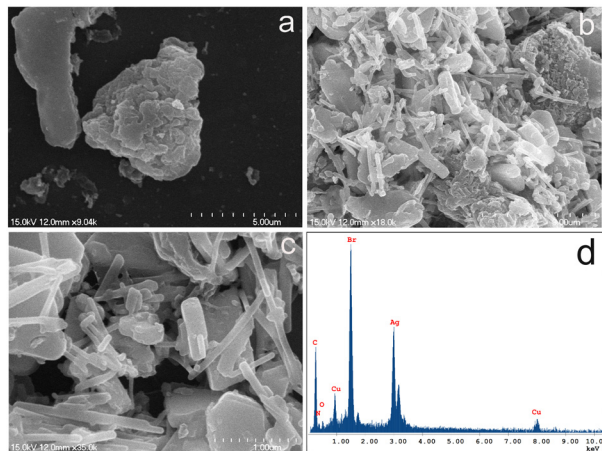
Fig. 2 SEM images of g-C_3N_4 (a) and **1**/g-C_3N_4 (b and c), and EDS spectrum of **1**/g-C_3N_4 (d).

are coordinated by four Br atoms to form the primary building unit (PBU) AgBr$_4$. Three AgBr$_4$ PBUs are interlinked by edge-sharing to form the secondary building unit (SBU) Ag$_3$Br$_7$ with a semi-cubic core Ag$_3$Br$_4$, in which three Ag atoms are capped by a μ_3-Br triple ligand (Fig. 3b). The Ag$_3$Br$_7$ SBUs are connected into a one-dimensional [Ag$_3$Br$_5$]$_n$ chain (Fig. 3c). In the [Ag$_3$Br$_5$]$_n$ chain, Ag$\cdots$Ag metal–metal interaction is observed between Ag(3) and Ag(3#1) with a Ag$\cdots$Ag separation of 3.0726(15) Å (Table S2†), which was consistent with those found in reported bromoargentate hybrids.[25a,26] All AgBr$_4$ PBUs had distorted tetrahedral geometries with Br–Ag–Br angles in the range of 94.51(3)–134.96(5)° (Table S2†). The Ag–Br bond lengths vary from 2.5827(11) Å to 2.8415(13) Å, and are consistent with those of the 1-D chains [Ag$_2$Br$_3$]$_n^{n-}$,[27] [Ag$_6$-Br$_{11}$]$_n^{5n-}$, [Ag$_{13}$Br$_{17}$]$_n^{4n-}$.[8a] The Cu^{2+}(1) and Cu^{2+}(2) ions are joined by two μ-OH bridging ligands and each Cu^{2+} ion is coordinated by a bidentate phen to form a [{Cu(phen)}$_2$(μ-OH)$_2$] unit (Fig. 3a). Two [{Cu(phen)}$_2$(μ-OH)$_2$] units are coupled by sharing the O2 atom to yield a tetranuclear [{Cu(phen)}$_2$(μ-

OH)$_2$]$_2$ complex unit (Fig. 4). The Cu(1) atom is further coordinated by a Br atom from the [Ag$_3$Br$_5$]$_n$ chains (Fig. 3a). As a result, acting as bridging linkers, the [{Cu(phen)}$_2$(μ-OH)$_2$]$_2$ complex units connect the [Ag$_3$Br$_5$]$_n$ chains into a [{Cu(phen)}$_2$(μ-OH)$_2$(Ag$_3$Br$_5$)]$_n$ layer *via* Cu(1)–Br(1) (Fig. 5). Both the Cu^{2+}(1) and Cu^{2+}(2) ions have distorted tetragonal pyramid geometries with the O$_2$N$_2$Br and O$_3$N$_2$ donor sets, respectively (Fig. 3d and e). The axial angles of the tetragonal pyramids are 161.3(2)° and 172.7(3)° for Cu(1)O$_2$N$_2$Br, and 164.9(3)° and 177.0(3)° for Cu(2)O$_3$N$_2$ (Table S2†). The Cu–Br, Cu–N, and Cu–O bond lengths are 2.9264(13) Å, 1.996(7)–2.024(6) Å and 1.919(5)–2.381(5) Å, respectively (Table S2†), which are consistent with the corresponding bond lengths reported in the literature.[25] The [{Cu(phen)}$_2$(μ-OH)$_2$(Ag$_3$Br$_5$)]$_n$ layers are perpendicular to the *a* axis of the unit cell. The planes of all the phen molecules are parallel, and the interplanar separations between the centroids of the phen molecules are in the range of 3.471–3.560 Å, indicating weak intermolecular $\pi\cdots\pi$ stacking interactions between the [{Cu(phen)}$_2$(μ-OH)$_2$(Ag$_3$Br$_5$)]$_n$ layers (Fig. S2†). The interplane separations are in the range of those of reported metal complexes with phen ligands.[28] The phen ligands further interact with the [Ag$_3$Br$_5$]$_n$ chains in neighboring [{Cu(phen)}$_2$(μ-OH)$_2$(Ag$_3$Br$_5$)]$_n$ layers through C–H$\cdots$Br hydrogen bonds (Fig. S3†). The C$\cdots$Br distances are in the range of 3.461–3.847 Å (Table S3†), which are consistent with those reported in organic bromoargentate hybrids.[7,29] The [{Cu(phen)}$_2$(μ-OH)$_2$(Ag$_3$Br$_5$)]$_n$ layers are connected into a 3-D framework *via* the $\pi\cdots\pi$ and C–H$\cdots$Br interactions.

Several bromoargentate hybrids that contain transition metal complex cations with phen or 2,2′-bipy organic ligands have been prepared and structurally characterized.[8a,25a] In these hybrids, the coordination sites of TM^{2+} ions are saturated by three phen or 2,2′-bipy ligands, and the bromoargentate aggregates cannot coordinate to the TM^{2+} ions. Examples include K[TM(2,2′-bipy)$_3$]$_2$Ag$_6$Br$_{11}$ (TM = Fe, Co, Ni, Zn), [TM(2,2′-bipy)$_3$]$_2$Ag$_{13}$Br$_{17}$,[8a] [TM(phen)$_3$]$_2$Ag$_{13}$-Br$_{17}$·2DMSO·3H$_2$O (TM = Fe, Co, Ni), [Cu(phen)$_2$(Br)]AgBr$_2$, and [Fe(phen)$_3$]Ag$_2$Br$_4$·DMF.[25a] In compound **1**, the Cu(1)$^{2+}$ ion forms a 4-coordinated center in the [{Cu(phen)}$_2$(μ-OH)$_2$]$_2$ complex units, thus, the [Ag$_3$Br$_5$]$^{2-}$ anion can bind to the Cu(1)$^{2+}$ center *via* the Br(1) atom to satisfy the coordination number 5 for the Cu^{2+} ion. Compound **1** represents the first example of a bromoargentate hybrid with a bromoargentate anion coordinating to the TM center *via* a TM–Br bond.
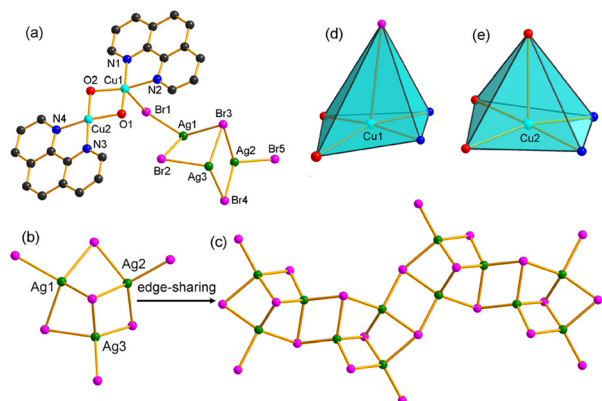
Fig. 3 Structural diagrams of **1**: asymmetric unit [{Cu(phen)}$_2$(μ-OH)$_2$(Ag$_3$Br$_5$)] of **1** with the labelling scheme (a), the trinuclear secondary building unit Ag$_3$Br$_7$ (b), the [Ag$_3$Br$_5$]$_n$ chain (c), and the tetragonal pyramid of Cu(1)O$_2$N$_2$Br (d) and Cu(2)O$_3$N$_2$ (e).

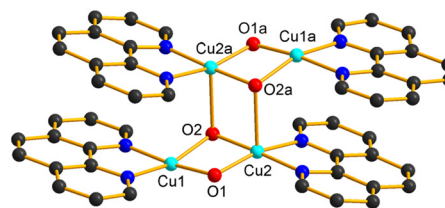**Fig. 4** Structure of the tetranuclear complex unit [{Cu(phen)}$_2$(μ-OH)$_2$]$_2$ in **1**. Hydrogen atoms are omitted for clarity.

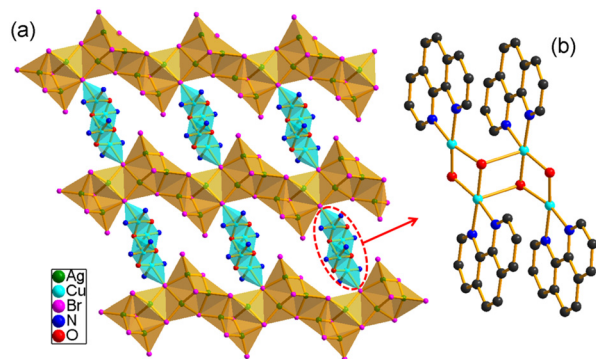**Fig. 5** Structural diagrams of **1**: the $[\{Cu(phen)\}_2(\mu\text{-}OH)_2(Ag_3Br_5)]_n$ layer in **1** viewed along the *a* axis (a), and the $\mu\text{-}[\{Cu(phen)\}_2(\mu\text{-}OH)_2]_2$ linkers between the $[Ag_3Br_5]_n$ chains (b). The carbon and hydrogen atoms in (a) are omitted for clarity. Yellow tetrahedra: $AgBr_4$. Cyan tetragonal pyramids: CuO_2N_2Br and CuO_3N_2.

Optical bandgaps and photocurrent responses

Solid state UV-vis-NIR reflectance spectra of the g-C_3N_4, **1**, and **1**/g-C_3N_4 heterojunction were measured using powder samples (Fig. S4†). The absorption spectra, which were converted from the reflectance data by the Kubelka–Munk function $F(R) = (1 - R)^2/2R$,[30] are shown in Fig. 6a. As shown in Fig. 6a, g-C_3N_4, **1**, and **1**/g-C_3N_4 exhibited well-defined abrupt absorption edges from which the band gap (E_g) can be estimated at 2.72 eV, 2.48 eV, and 2.58 eV, respectively. The band gap of the **1**/g-C_3N_4 heterojunction is greater than that of compound **1**, and lower than that of g-C_3N_4. When g-C_3N_4 was loaded, the absorption band gap of the **1**/g-C_3N_4 heterojunction underwent a blueshift compared to that of pure **1**. The band gap of **1**/g-C_3N_4 is smaller than that of
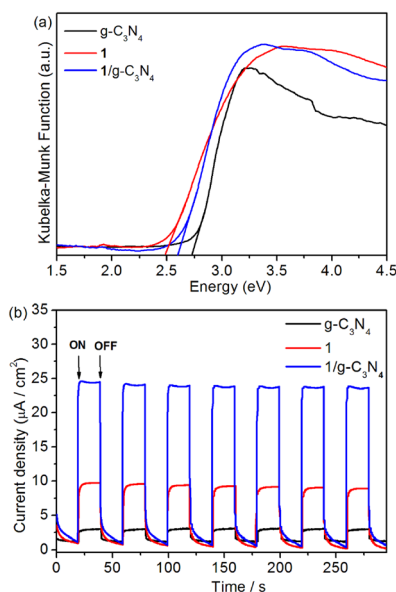
bromoargentate hybrids containing organic cations, such as $[H_2\text{-}DABCO][Ag_2Br_4(DABCO)]$ (E_g = 3.44 eV),[31] and $[H_3(DABCO)_2]Ag_3\text{-}Br_6$ (DABCO = 1,4-diazabicyclo[2.2.2]octane) (E_g = 4.20 eV).[32] However, these values are greater than those for the TM-complex containing bromoargentate hybrids $[TM(phen)_3]_2Ag_{13}\text{-}Br_{17}\cdot2DMSO\cdot3H_2O$ (phen = 1,10-phenanthroline) [E_g = 2.18 eV (Fe), 2.15 eV (Co), 2.24 eV (Ni)], $[Fe(phen)_3]Ag_2Br_4\cdot DMF$ (E_g = 2.19 eV),[25a] $[TM(phen)_3]PbAg_2Br_6$ [E_g = 1.99 eV (Fe), 2.74 eV (Ni)],[33] $[NH_4][Fe(2,2'\text{-}bipy)_3]_2[Ag_6Br_{11}]$ (E_g = 1.90 eV),[26] and iodoargentate hybrids $[TM(2,2'\text{-}bipy)_3]Ag_5I_7$ [E_g =1.94 eV(Co), 2.10 eV(Ni), 2.58 eV (Zn)],[34] and $K_x[TM(2,2'\text{-}bipy)_3]_2Ag_6I_{11}$ (x = 0.89–1) [E_g = 2.01 eV(Mn), 1.66 eV(Fe), 1.75 eV(Co), 1.85 eV(Ni), 2.08 eV(Zn)].[6]

The **1**/g-C_3N_4 heterojunction was photosensitive to visible light, and exhibited rapid photocurrent response under visible light illumination at room temperature. As shown in Fig. 6b, the photocurrent density of the **1**/g-C_3N_4 heterojunction increased dramatically once the light was turned on, and immediately decreased to approximately zero when the light was turned off. After illumination by Xe light at a power of 150 W, the photocurrent density of the **1**/g-C_3N_4 heterojunction was 24.58 $\mu A\ cm^{-2}$ in the first on/off switch, and stabilized at 23.68 $\mu A\ cm^{-2}$ after nine on/off switch cycles, indicating that the **1**/g-C_3N_4 heterojunction had a good reproducible photocurrent response. The **1**/g-C_3N_4 heterojunction exhibited much stronger photocurrent response than the pure compound **1** and g-C_3N_4. The pure compound **1** and g-C_3N_4 had steady photocurrent densities of 8.92 $\mu A\ cm^{-2}$ and 2.94 $\mu A\ cm^{-2}$, respectively, under the same visible light illumination. The current density of **1**/g-C_3N_4 is 2.65 and 8.05 times higher than those of pure **1** and g-C_3N_4, respectively. The enhanced photocurrent response suggested more effective separation of photogenerated carriers in the **1**/g-C_3N_4 heterojunction when it was illuminated by visible light. The doping of 2-D semiconducting material of g-C_3N_4 can promote the charge separation, and inhibit the recombination of photoexcited electrons and holes, therefore the photocurrent intensity is enhanced.[14,35] The stability of the photocurrent response of the **1**/g-C_3N_4 heterojunction was investigated by repeated measurements. As shown in Fig. S5,† the current intensities of the heterojunction were 26.08 and 24.92 $\mu A\ cm^{-2}$ in the first and second cycling measurements, respectively. The current intensity decreased slightly during the third cycle, and stabilized at 23.68 $\mu A\ cm^{-2}$ after three cycles, indicating the excellent photocurrent reproducibility and durability of the **1**/g-C_3N_4 heterojunction.

Photocatalytic properties

In the past twenty years, the discharge of harmful organic pollutants from industries has led to increasing water pollution. Photocatalysis is an environmentally friendly and economical sewage treatment method, that uses photogenerated electrons and holes on the surface of the catalyst to oxidize organic pollutants into nontoxic small molecules.[36] The photocatalytic behaviors of compound **1** and **1**/g-C_3N_4 heterojunction were evaluated by the model reaction of crystal violet (CV) photodegradation in aqueous solution under visible light

Fig. 6 (a) UV-vis-NIR absorption spectra of g-C_3N_4, **1** and **1**/g-C_3N_4. (b) Photocurrent densities of **1**, g-C_3N_4, and the **1**/g-C_3N_4 heterojunction under Xe light illumination at a power of 150 W.

irradiation. The change in the CV concentration was monitored by the intensity of the absorption maximum at a wavelength of 583 nm (Fig. S6†). The degradation efficiency was expressed as C_t/C_0, where C_0 and C_t are the initial and instantaneous concentrations of the dye, respectively. After the mixture of CV and the catalyst was stirred in the dark for 30 min, the adsorption between the catalyst and dye reached equilibrium, and approximately 10.6%, 6.0% and 7.6% of the dye was adsorbed on the g-C$_3$N$_4$, **1** and **1**/g-C$_3$N$_4$ heterojunction, respectively (Fig. S7†). The blank experiment showed that approximately 7.7% of CV was degraded in the absence of catalyst after light irradiation for 60 min. The degradation conversions of CV over g-C$_3$N$_4$ and **1** were 33.0% and 54.1%, respectively, after light irradiation for 60 min. The **1**/g-C$_3$N$_4$ heterojunction exhibited much more photocatalytic activity than g-C$_3$N$_4$ and compound **1**. In the presence of **1**/g-C$_3$N$_4$ heterojunction, the CV solution became almost colorless after 60 min of illumination, and the degradation conversion of CV reached 98.0% (Fig. 7a). The **1**/g-C$_3$N$_4$ heterojunction exhibited the highest degradation efficiency, which was in accordance with it having the strongest photocurrent response. The high photocurrent density implied efficient separation of photogenerated carriers,[37] and therefore, the photocatalytic activity was improved. As shown in Fig. 7b, the plot of Ln(C_0/C_t) against the irradiation time t fits the formula Ln(C_0/C_t) = kt, indicating that the photodegradation reactions catalyzed by g-C$_3$N$_4$, compound **1** and **1**/g-C$_3$N$_4$ heterojunction conform to first-order kinetics. The kinetic rate constants k of the degradation reactions are 0.0774, 0.0118, and 0.0519 min^{-1} for g-C$_3$N$_4$, **1** and **1**/g-C$_3$N$_4$, respectively. The **1**/g-C$_3$N$_4$ heterojunction

had the highest rate constant, which was 6.7 and 4.4 times greater than that of pure g-C$_3$N$_4$ and compound **1**, indicating the synergistic effect between **1** and g-C$_3$N$_4$ towards visible-light-driven photocatalytic performance in the degradation of CV. The **1**/g-C$_3$N$_4$ exhibited distinctly higher photocatalytic activity for CV degradation in comparison with the TM(II)-complex containing haloargentate hybrids [TM(phen)$_3$]$_2$Ag$_{13}$Br$_{17}$·2DMSO·3H$_2$O (TM = Fe, Co, Ni), [Cu(phen)$_2$(Br)]AgBr$_2$,[25a] [Ni(2,2′-bipy)$_3$][H-2,2-bipy]Ag$_2$I$_6$,[6] [Zn(2,2′-bipy)$_3$]Ag$_3$I$_5$,[11b] [Mn(2,2′-bipy)$_2$(DMF)$_2$]Ag$_5$I$_7$, and [{Zn(DMF)$_2$(H$_2$O)$_2$}(4,4′-bipy)$_{1.5}$]Ag$_5$I$_7$·2DMF.[38] The degradation ratios of CV on these haloargentate hybrid catalysts were in the range of 38–71% after light irradiation for 60 min. The **1**/g-C$_3$N$_4$ heterojunction also showed higher ocatalytic activity than did the MOF/g-C$_3$N$_4$ composites of NH$_2$-MIL-88B(Fe)/g-C$_3$N$_4$ (NH$_2$-MIL = 2-aminoterephthalic acid), and Ce-BTC/g-C$_3$N$_4$ (H$_3$BTC = 1,3,5-benzenetricarboxylic acid) in degradation of organic dyes.[39] Approximately 58% and 73% of MB dye were degraded on the two MOF/g-C$_3$N$_4$ composites, respectively, after light irradiation for 60 min.

After the photocatalytic reaction, the catalyst samples of compound **1** and the **1**/g-C$_3$N$_4$ heterojunction were collected by centrifugation for powder X-ray diffraction measurements. The PXRD patterns of the catalysts were basically the same as those of the as-prepared sample, with the position of the diffraction peaks unchanged (Fig. S8†), indicating that the catalyst samples had good structural stability during photodegradation. The photocatalytic stability and durability of the photocatalyst are important aspects of its practical application. The catalytic stability of the **1**/g-C$_3$N$_4$ heterojunction was investigated by repeated experiments. As shown in Fig. 8a, the **1**/g-C$_3$N$_4$ heterojunction exhibited relatively steady photocatalytic activities in five consecutive cycles. The photocatalytic ratio remains at 93% after five catalytic cycles in the degradation of CV.

Possible photodegradation mechanism

It is generally believed that photoinduced superoxide (·O$_2$$^-$) and hydroxyl radicals (·OH), and positive holes (h$^+$) are active substances for the photocatalytic degradation of organic pollutants in aqueous solution. Benzoquinone (BQ), *tert*-butanol (TBA), and ammonium oxalate (AO) which are quenchers of ·O$_2$$^-$ and ·OH radicals, and h$^+$ holes, respectively, were added to the photocatalytic reaction to explore the reactive species during the photodegradation of CV catalyzed by the **1**/g-C$_3$N$_4$ heterojunction. As shown in Fig. 8b and S9,† all the degradation ratios of CV over the **1**/g-C$_3$N$_4$ heterojunction decreased when BQ, AO and TBA were added to the catalytic reaction. The degradation ratios decreased from 98.0% without quenchers to 29.2%, 25.1%, and 46.9% in the presence of BQ, AO and TBA, respectively, after light irradiation for 60 min (Fig. 8b), indicating that all h$^+$, ·O$_2$$^-$, and ·OH radicals are the reactive species during the degradation on the **1**/g-C$_3$N$_4$ heterojunction.

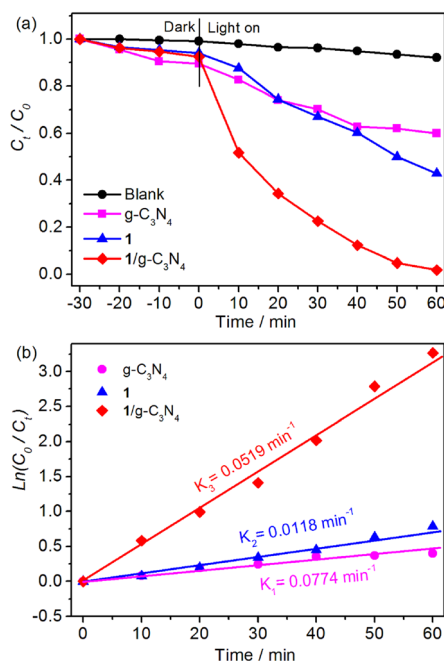The oxidation ability of photogenerated holes of photocatalysts can be determined by the energy of the

Fig. 7 (a) Photocatalytic activities in CV degradation over g-C$_3$N$_4$, **1**, and **1**/g-C$_3$N$_4$ heterojunction. (b) Linear relationship of Ln(C_0/C_t) *versus* reaction time t over g-C$_3$N$_4$, **1**, and **1**/g-C$_3$N$_4$ heterojunction during the photodegradation of CV.
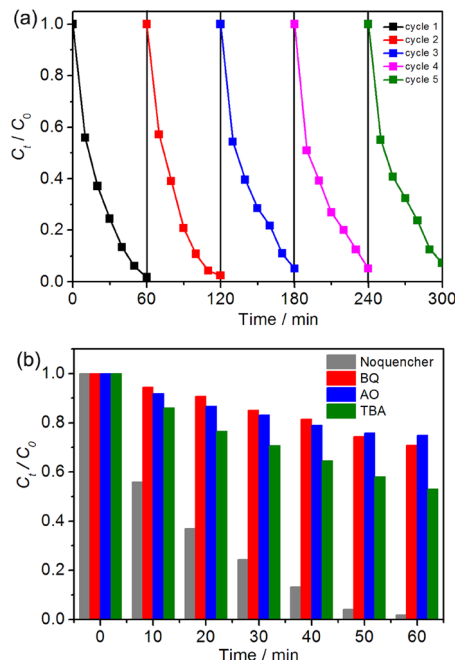
Fig. 8 (a) Degradation ratio of CV over the **1**/g-C3N4 heterojunction in cycling tests. (b) Degradation ratios of CV over **1**/g-C3N4 heterojunction in the presence of the BQ, AO and TBA quenchers.

valence band.[40] The potentials of the valence band (E_{VB}) and conduction band (E_{CB}) of g-C_3N_4 are 1.50 eV and −1.22 eV, respectively.[41] The VB XPS spectrum showed that the valence band edge of **1** is located at 1.03 eV (Fig. S10†), and therefore the conduction band edge of **1** is located at −1.45 eV. The **1**/g-C_3N_4 hybrid is a typical type II heterojunction based on the potentials of the valence and conduction bands of g-C_3N_4 and **1** (Fig. 9).[14c,42] When the **1**/g-C_3N_4 heterojunction is irradiated by visible light, photogenerated electrons are generated in the conduction band (CB) and positive holes (h^+) remain in the valence band (VB) (eqn (1)).[43] The photogenerated electrons on the CB of **1** can jump to the less negative CB of g-C_3N_4, while the h^+ holes in the VB of g-C_3N_4 move to the VB of **1** in the **1**/g-C_3N_4 heterojunction (eqn (2), (3) and Fig. 9). The doping of g-C_3N_4 on **1** can effectively promote the charge separation, and minimize the recombination of the electron–hole pairs. The holes on the VB of **1** could react with water to produce extremely reactive hydroxyl radicals (·OH) as shown in eqn (4), or directly participate in the oxidization of the organic dye, whereas the electrons on the CB of g-C_3N_4 could combine with oxygen to form the superoxide radical ·O_2^- according to eqn (5).[43] The formation of a type II heterojunction by doping g-C_3N_4 leads to the migration of charge carriers in the opposite direction.[14c,44] This significantly enhances the electron–hole spatial separation on various parts of the heterojunction to prevent the charge recombination, and to prolong the lifetime of free electrons and holes, which is helpful for the generation of reactive species h^+, ·OH and ·O_2^- on the surface of the heterojunction. The synergistic effect of the three h^+, ·O_2^-, and ·OH reactive species accounts for the much higher
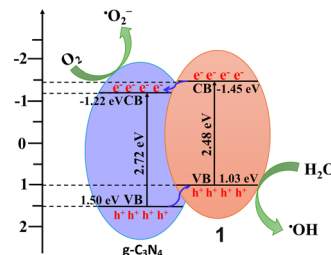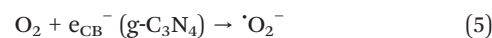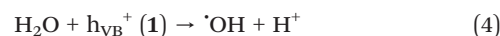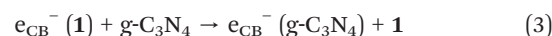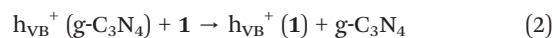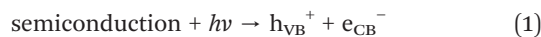

Fig. 9 Schematic diagram illustrating the photocatalytic mechanism for CV degradation over the **1**/g-C3N4 heterojunction under visible light irradiation.

degradation rate of the **1**/g-C_3N_4 heterojunction than that of pure **1** and g-C_3N_4 during the photodegradation of CV.

$$\text{semiconduction} + h\nu \rightarrow h_{VB}^+ + e_{CB}^- \tag{1}$$

$$h_{VB}^+ (\text{g-}C_3N_4) + \mathbf{1} \rightarrow h_{VB}^+ (\mathbf{1}) + \text{g-}C_3N_4 \tag{2}$$

$$e_{CB}^- (\mathbf{1}) + \text{g-}C_3N_4 \rightarrow e_{CB}^- (\text{g-}C_3N_4) + \mathbf{1} \tag{3}$$

$$H_2O + h_{VB}^+ (\mathbf{1}) \rightarrow {}^{\cdot}OH + H^+ \tag{4}$$

$$O_2 + e_{CB}^- (\text{g-}C_3N_4) \rightarrow {}^{\cdot}O_2^- \tag{5}$$

Conclusions

In summary, a 2-D bromoargentate hybrid $[\{Cu(phen)\}_2(\mu\text{-}OH)_2(Ag_3Br_5)]_n$ (**1**) was prepared in a C_2H_5OH/DMF mixed solvent under solvothermal conditions. The $[\{Cu(phen)\}_2(\mu\text{-}OH)_2(Ag_3Br_5)]_n$ layers were successfully loaded on the surface of g-C_3N_4 heterojunction by *in situ* growth under the same solvothermal conditions, and **1**/g-C_3N_4 heterojunction was obtained. The **1**/g-C_3N_4 heterojunction performed a stable and reproducible photocurrent response. Its photocurrent density is 2.65 and 8.05 times higher than those of parent **1** and g-C_3N_4, respectively, indicating that the formation of heterojunction is helpful for the separation of photogenerated carriers, therefore, the photocurrent intensity is enhanced. The improved photocatalytic efficiency of the **1**/g-C_3N_4 heterojunction compared to that of parent **1** and g-C_3N_4 demonstrated the excellent synergistic effect of the **1**/g-C_3N_4 heterojunction cocatalyst on CV degradation. This result showed that new efficient visible-light photocatalysts can be obtained by the rational design and construction of g-C_3N_4-based heterogeneous heterojunctions with the aim of promising applications in the area of solar energy conversion and environmental remediation.

Experimental section

Materials and methods

The g-C_3N_4 sample was prepared by thermal polymerization using urea as the precursor according to a previously reported

method.[45] 1.5 g of urea was ground evenly placed in a ceramic crucible, heated to 550 °C at a heating rate of 5 °C min^{-1} in a muffle furnace and kept at 550 °C for 4 h. A faint yellow product of g-C_3N_4 was obtained after cooling to room temperature. All other chemicals ($Cu(NO_3)_2 \cdot 3H_2O$, AgBr, KBr, phen, *tert*-butyl alcohol (TBA), 1,4-benzoquinone (BQ), ammonium oxalate (AO), crystal violet (CV), C_2H_5OH, and DMF) were purchased from McLean Chemical Reagents Co., Ltd. (Shanghai, China). All of the chemicals used in the experiments were of analytical grade and used without any further purification. Physical and chemical measurements and characterizations, including elemental analysis, FT-IR, powder X-ray diffraction (PXRD), scanning electron microscopy (SEM), X-ray energy dispersive spectroscopy (EDS), X-ray photoelectron spectroscopy (XPS), solid-state UV-vis reflectance spectroscopy, photocurrent response measurements, and photocatalytic tests, are provided in the ESI.†

Syntheses

Synthesis of [{Cu(phen)}$_2$(μ-OH)$_2$(Ag$_3$Br$_5$)]$_n$ (1). $Cu(NO_3)_2 \cdot 3H_2O$ (242 mg, 1.0 mmol), AgBr (282 mg, 1.5 mmol), KBr (298 mg, 2.5 mmol) and phen (270 mg, 1.5 mmol) were mixed in 4 ml of C_2H_5OH and 2 ml of DMF under stirring. After being ultrasonically dispersed for 10 min, the mixture was transferred to a polytetrafluoroethylene (PTFE)-lined stainless steel autoclave with a volume of 15 mL. The sealed autoclave was heated at 110 °C for 5 days, and then naturally cooled to room temperature. The blue block crystals were collected by filtration, washed with ethanol, and stored under vacuum (yield: 448 mg, 72% based on AgBr). Anal. calcd. for $C_{24}H_{18}N_4O_2Cu_2Ag_3Br_5$ (**1**): C, 23.16; H, 1.46; N, 4.50. Found: C, 22.91; H, 1.39; N, 4.39%. IR (KBr, cm^{-1}): 3578 (br, m), 3447 (m), 3068 (m), 2949 (m), 2881 (m), 1608 (m), 1576 (m), 1523 (w), 1439 (s), 1376 (s), 1291 (m), 1173 (w), 1088 (w), 978 (w), 909 (w), 828 (w), 759 (s), 647 (m).

Synthesis of the 1/g-C_3N_4 heterojunction. g-C_3N_4 (46 mg), $Cu(NO_3)_2 \cdot 3H_2O$ (121 mg, 0.50 mmol), AgBr (141 mg, 0.75 mmol), KBr (149 mg, 1.25 mmol) and phen (135 mg, 1.25 mmol) were mixed in 2 ml of C_2H_5OH and 1 ml of DMF under stirring. After being ultrasonically dispersed for 30 min, the mixture was transferred to a PTFE-lined stainless steel autoclave with a volume of 15 mL. The sealed autoclave was heated at 110 °C for 3 days. After cooling to room temperature, powder product was washed with ethanol and **1**/g-C_3N_4 heterojunction was obtained. IR (KBr, cm^{-1}): 3433 (br, m), 3070 (m), 2920 (w), 2881 (w), 1626 (m), 1574 (m), 1525 (s), 1457 (m), 1435 (m),1395 (s), 1314 (s), 1233 (s), 1202 (s), 1086 (m), 1000 (w), 889 (w), 805 (m), 759 (s), 647 (m).

X-ray crystal structure determination

The data of compound **1** were collected on a Bruker CCD diffractometer using graphite-monochromated Mo-Kα radiation with an ω-scan method to a maximum 2θ value of 50.70°. An empirical absorption correction was conducted for all the crystals by using the multi-scan method. The structure was solved by SHELXS-14.[46a] and refinement was performed against F^2 using SHELXL-14.[46b] All the nonhydrogen atoms were refined anisotropically. The hydrogen atoms were positioned with an idealized geometry and refined using the riding model. The technical details of the data acquisition and selected refinement results are summarized in Table S1.†

Data availability statement

All relevant data are within the manuscript and its ESI.†

Author contributions

Yiming Tian: investigation, methodology, formal analysis, and writing. Taohong Ren: investigation, and methodology. Hongjin Zhu: investigation. Dingxian Jia: conceptualization, methodology, writing – review and editing, supervision, and project administration.

Conflicts of interest

The authors declare no competing financial interest.

Acknowledgements

References

1 (*a*) B. J. Sánchez and J. Wang, *Environ. Sci.: Nano*, 2018, **5**, 1530–1544; (*b*) V. K. Sharma, X. M. Ma and R. Zboril, *Chem. Soc. Rev.*, 2023, **52**, 7673–7686.

2 R. Das, C. D. Vecitis, A. Schulze, B. Cao, A. F. Ismail, X. B. Lu, J. P. Chen and S. Ramakrishna, *Chem. Soc. Rev.*, 2017, **46**, 6946–7020.

3 (*a*) H. X. Mai, D. H. Chen, Y. Tachibana, H. Suzuki, R. Abe and R. A. Caruso, *Chem. Soc. Rev.*, 2021, **50**, 13692–13729; (*b*) J. Wang, N. Licciardello, M. Sgarzi and G. Cuniberti, *Nanoscale Adv.*, 2024, **6**, 1653–1660; (*c*) Z. B. Wang, H. B. Wang, P. Wang, X. W. Liu, X. F. Lei, R. Guo, J. H. You and H. Z. Zhang, *Coord. Chem. Rev.*, 2024, **499**, 215506.

4 G. N. Liu, X. Zhang, H. M. Wang, H. Xu, Z. H. Wang, X. L. Meng, Y. N. Dong, R. Y. Zhao and C. C. Li, *Dalton Trans.*, 2017, **46**, 12474–12486.

5 C. Y. Yue, B. Hu, X. W. Lei, R. Q. Li, F. Q. Mi, H. Gao, Y. Li, F. Wu, C. L. Wang and N. Lin, *Inorg. Chem.*, 2017, **56**, 10962–10970.

6 X. W. Lei, C. Y. Yue, J. Q. Zhao, Y. F. Han, J. T. Yang, R. R. Meng, C. S. Gao, H. Ding, C. Y. Wang, W. D. Chen and M. C. Hong, *Inorg. Chem.*, 2015, **54**, 10593–10603.

7 T. L. Yu, Y. B. Fu, Y. L. Wang, P. F. Hao, J. J. Shen and Y. L. Fu, *CrystEngComm*, 2015, **17**, 8752–8761.

8 (*a*) C. Y. Yue, X. W. Lei, Y. F. Han, X. X. Lu, Y. W. Tian, J. Xu, X. F. Liu and X. Xu, *Inorg. Chem.*, 2016, **55**, 12193–12203; (*b*) B. Zhang, J. Li, Y. Yang, W. H. Wang, H. Y. Shen and Y. N. Shao, *Dalton Trans.*, 2022, **51**, 13361–13367; (*c*) C. Y. Yue, X. W. Lei, X. X. Lu, Y. Li, J. C. Wei, W. Wang, Y. D. Yin and

N. Wang, *Dalton Trans.*, 2017, **46**, 9235–9244; (*d*) M. Daub and H. Hillebrecht, *Chem. – Eur. J.*, 2018, **24**, 9075–9082; (*e*) A. H. Coffey, P. Yoo, D. H. Kim, Akriti, M. Zeller, S. Avetian, L. Huang, P. Liao and L. Dou, *Chem. – Eur. J.*, 2020, **26**, 6599–6607.

9 (*a*) L. M. Wu, X. T. Wu and L. Chen, *Coord. Chem. Rev.*, 2009, **253**, 2787–2804; (*b*) N. Mercier, N. Louvain and W. H. Bi, *CrystEngComm*, 2009, **11**, 720–734; (*c*) J. S. Manser, J. A. Christians and P. V. Kamat, *Chem. Rev.*, 2016, **116**, 12956–13008.

10 (*a*) T. L. Yu, J. J. Shen, Y. L. Wang and Y. L. Fu, *Eur. J. Inorg. Chem.*, 2015, 1989–1996; (*b*) G. N. Liu, K. Li, Q. S. Fan, H. Sun, X. Y. Li, X. N. Han, Y. Li, Z. W. Zhang and C. C. Li, *Dalton Trans.*, 2016, **45**, 19062–19071; (*c*) M. H. Liu, W. Y. Wen, H. Y. Shao, Y. Yang, J. Li and B. Zhang, *Dalton Trans.*, 2024, **53**, 2991–2997; (*d*) X. W. Pan, L. Zhai, J. Zhang and X. M. Ren, *Inorg. Chem.*, 2024, **63**, 2640–2646.

11 (*a*) Y. L. Shen, J. L. Lu, C. Y. Tang, F. Wang, Y. Zhang and D. X. Jia, *RSC Adv.*, 2014, **4**, 39596–39605; (*b*) X. W. Lei, C. Y. Yue, J. Q. Zhao, Y. F. Han, Z. R. Ba, C. Wang, X. Y. Liu, Y. P. Gong and X. Y. Liu, *Eur. J. Inorg. Chem.*, 2015, **26**, 4412–4419; (*c*) X. W. Lei, C. Y. Yue, L. J. Feng, Y. F. Han, R. R. Meng, J. T. Yang, H. Ding, C. S. Gao and C. Y. Wang, *CrystEngComm*, 2016, **18**, 427–436; (*d*) Y. Mu, D. Wang, X. D. Meng, J. Pan, S. D. Han and Z. Z. Xue, *Cryst. Growth Des.*, 2020, **20**, 1130–1138; (*e*) C. Y. Tang, J. Yao, Y. Y. Li, Z. R. Xia, J. B. Liu and C. Y. Zhang, *Inorg. Chem.*, 2020, **59**, 13962–13971.

12 (*a*) W. Fang, C. Y. Tang, R. H. Chen, D. X. Jia, W. Q. Jiang and Y. Zhang, *Dalton Trans.*, 2013, **42**, 15150–15158; (*b*) P. F. Hao, W. Q. Wang, J. J. Shen and Y. L. Fu, *Dalton Trans.*, 2020, **49**, 8883–8890; (*c*) Y. Gao, N. N. Chen, Y. M. Tian, J. H. Zhang and D. X. Jia, *Inorg. Chem.*, 2021, **60**, 3761–3772.

13 F. Goettmann, A. Fischer, M. Antonietti and A. Thomas, *Chem. Commun.*, 2006, 4530–4532.

14 (*a*) X. C. Wang, S. Blechert and M. Antonietti, *ACS Catal.*, 2012, **2**, 1596–1606; (*b*) Y. Wang, X. C. Wang and M. Antonietti, *Angew. Chem., Int. Ed.*, 2012, **51**, 68–89; (*c*) W. J. Ong, L. L. Tan, Y. H. Ng, S. T. Yong and S. P. Chai, *Chem. Rev.*, 2016, **116**, 7159–7329; (*d*) S. Patnaik, A. Behera and K. Parida, *Catal. Sci. Technol.*, 2021, **11**, 6018–6040; (*e*) N. Sun, Y. Liang, X. J. Ma and F. Chen, *Chem. – Eur. J.*, 2017, **23**, 15466–15473; (*f*) A. Naseri, M. Samadi, A. Pourjavadi, A. Z. Moshfegh and S. Ramakrishn, *J. Mater. Chem. A*, 2017, **5**, 23406–23433.

15 (*a*) M. J. Bojdys, J. O. Müller, M. Antonietti and A. Thomas, *Chem. – Eur. J.*, 2008, **14**, 8177–8182; (*b*) W. Iqbal, B. C. Qiu, J. Y. Lei, L. Z. Wang, J. L. Zhang and M. Anpo, *Dalton Trans.*, 2017, **46**, 10678–10684.

16 (*a*) L. B. Jiang, X. Z. Yuan, Y. Pan, J. Liang, G. M. Zeng, Z. B. Wu and H. Wang, *Appl. Catal., B*, 2017, **217**, 388–406; (*b*) V. V. Phatake and B. M. Bhanage, *Catal. Lett.*, 2019, **149**, 347–359; (*c*) Q. Chen, J. F. Huang, T. Xiao, L. Y. Cao, D. H. Liu, X. Y. Li, M. F. Niu, G. T. Xu, K. Kajiyoshi and L. L. Feng, *Dalton Trans.*, 2023, **52**, 7447–7456.

17 (*a*) J. Liu, X. X. Zhao, P. Jing, W. Shi and P. Cheng, *Chem. – Eur. J.*, 2019, **25**, 2330–2336; (*b*) Z. F. Jiang, W. M. Wan,

H. M. Li, S. Q. Yuan, H. J. Zhao and P. K. Wong, *Adv. Mater.*, 2018, **30**, 1706108; (*c*) J. W. Wang, X. J. Zuo, W. Cai, J. W. Sun, X. L. Ge and H. Zhao, *Dalton Trans.*, 2018, **47**, 15382–15390; (*d*) Y. Y. Li, J. F. Shen, W. X. Quan, Y. Diao, M. J. Wu, B. Zhang, Y. Q. Wang and D. F. Yang, *Eur. J. Inorg. Chem.*, 2020, 3852–3858.

18 (*a*) S. Y. Yu, R. D. Webster, Y. Zhou and X. L. Yan, *Catal. Sci. Technol.*, 2017, **7**, 2050–2056; (*b*) W. W. Li, Y. J. Li, C. Yang, Q. X. Ma, K. Tao and L. Han, *Dalton Trans.*, 2020, **49**, 14017–14029; (*c*) R. Y. Zhang, K. Huang, H. H. Wei, D. Wang, G. Ou, N. Hussain, Z. Y. Huang, C. Zhang and H. Wu, *Dalton Trans.*, 2018, **47**, 1417–1421; (*d*) A. Q. Zhu, L. L. Qiao, Z. Q. Jia, P. F. Tan, Y. Liu, Y. J. Ma and J. Pan, *Dalton Trans.*, 2017, **46**, 17032–17040; (*e*) J. H. Ding, Y. J. Wang, S. H. Guo, Y. Z. Zhang, X. Xin, S. W. Tang, S. B. Liu and X. H. Li, *Eur. J. Inorg. Chem.*, 2021, 3719–3726.

19 S. K. Sharma, A. Kumar, G. Sharma, T. T. Wang, A. I. Juez and P. Dhiman, *J. Mol. Liq.*, 2023, **382**, 121890.

20 A. H. Cao, L. J. Zhang, Y. Wang, H. J. Zhao, H. Deng, X. M. Liu, Z. Lin, X. T. Su and F. Yue, *ACS Sustainable Chem. Eng.*, 2019, **7**, 2492–2499.

21 (*a*) P. Qiu, X. Y. Liao, Y. Jiang, Y. Yao, L. Shi, S. X. Lu and Z. Li, *New J. Chem.*, 2022, **46**, 20711–20722; (*b*) H. Sepehrmansourie, H. Alamgholiloo, M. A. Zolfigol, N. N. Pesyan and M. M. Rasooll, *ACS Sustainable Chem. Eng.*, 2023, **11**, 3182–3193.

22 N. N. Chen, Y. M. Tian, J. H. Zhang, X. Yang and D. X. Jia, *Inorg. Chem.*, 2022, **61**, 3317–3326.

23 J. Fu, B. B. Chang, Y. L. Tian, F. N. Xi and X. P. Dong, *J. Mater. Chem. A*, 2013, **1**, 3083–3090.

24 M. W. Kadi, R. M. Mohamed, A. A. Ismail and D. W. Bahnemann, *Appl. Nanosci.*, 2020, **10**, 223–232.

25 (*a*) Y. L. Shen, L. M. Zhang, S. F. Li, P. P. Sun, W. Q. Jiang and D. X. Jia, *Eur. J. Inorg. Chem.*, 2018, 826–834; (*b*) K. Gogoi, H. Deka, V. Kumar and B. Mondal, *Inorg. Chem.*, 2015, **54**, 4799–4805.

26 B. Zhang, J. Li, X. Chen, M. F. Yang, H. Y. Shen and J. C. Zhu, *Inorg. Chem. Commun.*, 2022, **137**, 109250.

27 T. L. Yu, G. X. Wu, M. Xue, Z. H. Wang and Y. L. Fu, *Dalton Trans.*, 2018, **47**, 12172–12180.

28 F. Gándara, C. F. Revilla, N. Snejko, E. G. Puebla, M. Iglesias and M. A. Monge, *Inorg. Chem.*, 2006, **45**, 9680–9687.

29 Y. B. Lu, L. Z. Cai, J. P. Zou, X. Liu, G. C. Guo and J. S. Huang, *CrystEngComm*, 2011, **13**, 5724–5729.

30 W. W. M. Wendlandt and H. G. Hecht, *Reflectance Spectroscopy*, Interscience Publishers, New York, 1966, p. 306.

31 C. Sun, Y. H. Guo, Y. Yuan, W. X. Chu, W. L. He, H. X. Che, Z. H. Jing, C. Y. Yue and X. W. Lei, *Inorg. Chem.*, 2020, **59**, 4311–4319.

32 R. C. Zhang, J. J. Wang, B. Q. Yuan, J. C. Zhang, L. Zhou, H. B. Wang, D. J. Zhang and Y. L. An, *Inorg. Chem.*, 2016, **55**, 11593–11599.

33 X. C. Ren, J. Li, W. H. Wang, Y. N. Shao, B. Zhang and L. Z. Li, *J. Solid State Chem.*, 2022, **308**, 122912.

34 X. W. Lei, C. Y. Yue, F. Wu, X. Y. Jiang and L. N. Chen, *Inorg. Chem. Commun.*, 2017, **77**, 64–67.

35 F. He, Z. X. Wang, Y. X. Li, S. Q. Peng and B. Liu, *Appl. Catal., B*, 2020, **269**, 118828.

36 (*a*) H. Tong, S. X. Ouyang, Y. P. Bi, N. Umezawa, M. Oshikiri and J. H. Ye, *Adv. Mater.*, 2012, **24**, 229–251; (*b*) J. R. Liu, H. Chen, X. J. Shi, S. Nawar, J. G. Werner, G. S. Huang, M. M. Ye, D. A. Weitz, A. A. Solovev and Y. F. Mei, *Environ. Sci.: Nano*, 2020, **7**, 656–664.

37 T. Hisatomi, J. Kubota and K. Domen, *Chem. Soc. Rev.*, 2014, **43**, 7520–7535.

38 W. Zheng, Y. Gao, N. N. Chen, B. Wu, D. X. Jia and S. X. Zhao, *Inorg. Chim. Acta*, 2020, **510**, 119762.

39 (*a*) Z. Durmus, R. Köferstein, T. Lindenberg, F. Lehmann, D. Hinderberger and A. W. Maijenburg, *Ceram. Int.*, 2023, **49**, 24428–24441; (*b*) X. Y. Li, Y. H. Pi, L. Q. Wu, Q. B. Xia, J. L. Wu, Z. Li and J. Xiao, *Appl. Catal., B*, 2017, **202**, 653–663.

40 (*a*) W. T. Xu, L. Ma, F. Ke, F. M. Peng, G. S. Xu, Y. H. Shen, J. F. Zhu, L. G. Qiu and Y. P. Yuan, *Dalton Trans.*, 2014, **43**, 3792–3798; (*b*) T. V. Vua, A. A. Lavrentyev, B. V. Gabrelian, H. D. Tong, V. A. Tkach, O. V. Parasyuk and O. Y. Khyzhun, *Opt. Mater.*, 2019, **96**, 109296; (*c*) P. Qiu, Y. Yao, S. X. Lu, L. G. Chen, Y. Y. Chen and X. Y. Liao, *Fuel*, 2023, **351**, 129043.

41 Z. H. Xu, B. T. Xu, K. Qian, Z. Li, F. Ding, M. M. Fan, Y. G. Sun and Y. Gao, *RSC Adv.*, 2019, **9**, 25638–25646.

42 M. Majdoub, Z. Anfar and A. Amedlous, *ACS Nano*, 2020, **14**, 12390–12469.

43 (*a*) A. S. Weber, A. M. Grady and R. T. Koodali, *Catal. Sci. Technol.*, 2012, **2**, 683–693; (*b*) J. F. Qu, D. Y. Chen, N. J. Li, Q. F. Xu, H. Li, J. H. He and J. M. Lu, *Appl. Catal., B*, 2019, **256**, 117877.

44 R. Marschall, *Adv. Funct. Mater.*, 2014, **24**, 2421–2440.

45 J. H. Liu, T. K. Zhang, Z. C. Wang, G. Dawson and W. Chen, *J. Mater. Chem.*, 2011, **21**, 14398–14401.

46 G. M. Sheldrick, *SHELXS-14, Program for structure solution*, University of Göttingen, Germany, 2014; G. M. Sheldrick, *SHELXL-14, Program for structure refinement*, University of Göttingen, Germany, 2014.